Tunable quantum temperature oscillations in graphene nanostructures

Justin P. Bergfield, Mark A. Ratner, Charles A. Stafford, and Massimiliano Di Ventra

Phys. Rev. B **91**, 125407 — Published 5 March 2015

DOI: 10.1103/PhysRevB.91.125407

Tunable Quantum Temperature Oscillations in Graphene Nanostructures

Justin P. Bergfield and Mark A. Ratner
*Department of Chemistry, Northwestern University, 2145 Sheridan Road, Evanston, IL, 60208**

Charles A. Stafford
Department of Physics, University of Arizona, 1118 East Fourth Street, Tucson, AZ 85721

Massimiliano Di Ventra
Department of Physics, University of California, San Diego, La Jolla, CA 92093

We investigate the local electron temperature distribution in graphene nanoribbon (GNR) and graphene junctions subject to an applied thermal gradient. Using a realistic model of a scanning thermal microscope, we predict quantum temperature oscillations whose wavelength is related to that of Friedel oscillations. Experimentally, this wavelength can be tuned over several orders of magnitude by gating/doping, bringing quantum temperature oscillations within reach of the spatial resolution of existing measurement techniques.

PACS numbers: 72.80.Vp,68.37.Hk,05.30.Fk

Nanometer resolution temperature measurements are technologically necessary, for instance, to characterize the thermal performance and failure mechanisms of semiconductor devices[1], or to investigate bioheat transfer at the molecular level for the treatment of cancer or cardiovascular diseases[2]. Fundamentally, local temperature measurements of quantum systems can elucidate the correspondence between phonon[3–5], photon[6–8], and electron temperature[9–12] measures. Moreover, quantum effects may offer novel methods to circumvent long-standing technological challenges, suggesting that the investigation of 'phase sensitive'[13] thermal effects could open the door to quantum engineered heat transport devices[14,15].

Quantum coherent temperature oscillations have been predicted in 1-D ballistic systems[16,17] and in small conjugated organic molecules[11], but despite impressive advances in thermal microscopy[18–21] that have dramatically increased the spatial resolution of temperature measurements, these predictions are not yet within reach of experimental verification.

In this letter, we investigate the local electron temperature distribution of graphene nanoribbon (GNR) and graphene junctions covalently bonded to two metallic electrodes used to apply a thermal bias, and probed using a third scanning electrode acting as a local thermometer. We find that the Friedel oscillations (an equilibrium property) and temperature oscillations (a non-equilibrium transport effect) in these systems are related, in that techniques to modify the former[22] can also be used to modify the latter. Specifically, we investigate the response of junctions to an applied gate voltage and find that the temperature oscillation wavelength can be varied over several orders of magnitude, bringing these oscillations within the spatial resolution of current techniques in thermal microscopy[18–21].

Theory – Defining a local electronic temperature in a system out of equilibrium requires consideration of a local probe (thermometer) that couples to the system and whose temperature is varied until the local properties of the system are minimally perturbed[16,17,23]—a floating probe. This should occur when the thermometer reaches *local equilibrium* with the system, i.e., when there is no longer any net flow of charge or heat between the system and the probe[11]. Several variations on the later condition have also been discussed in the literature[9,24–26].

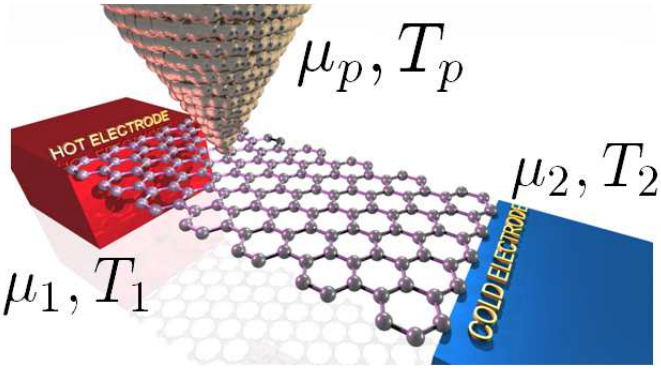

FIG. 1. A schematic representation of a three terminal GNR junction with the hot and cold electrodes covalently bonded to the GNR and a third scanning thermal probe positioned over the GNR. The probe is allowed to come into thermal and electrical equilibrium with the sample and measure the temperature T_p.

We consider junctions composed of a GNR or graphene sheet, hot and cold electrodes bonded to the system, a probe electrode, and the environment (see Fig. 1). The hot and cold electrodes provide a thermal gradient, but form an open electrical circuit in a thermal transport experiment. Under these conditions, and in linear response, the heat current flowing into the scanning thermal probe is

$$I_p^Q = \sum_{\beta=1}^{2} \tilde{\kappa}_{p\beta}(T_\beta - T_p) + \kappa_{p0}(T_0 - T_p) + \kappa_{ph}(T_{ph} - T_p), \quad (1)$$

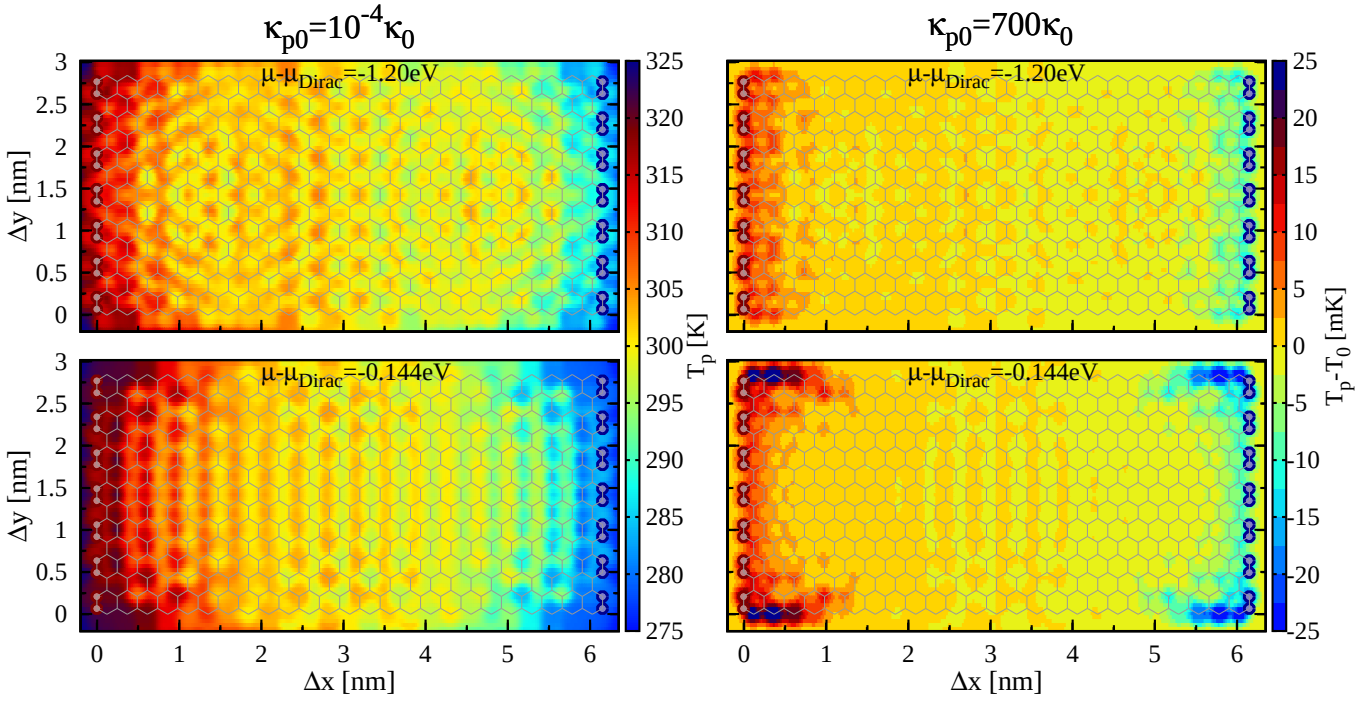

FIG. 2. The calculated spatial temperature profile for a zig-zag GNR probed by a Pt SThM fixed 2.5Å above the sheet shown for two energies and for weak and strong environmental coupling with κ_{p0}=$10^{-4}\kappa_0$ and κ_{p0}=$700\kappa_0$, respectively. In all panels phonons are included with κ_{ph}=$0.01\kappa_0$. By adjusting $|\mu-\mu_{\rm Dirac}|$ the temperature oscillation wavelength can be tuned. Even with strong environmental coupling and significant phonon heat conductance, the quantum temperature oscillations are visible. The phonon temperature T_{ph} is taken to vary linearly between each electrode and the applied temperature gradient across the nanoribbon is 50K.

where T_β is the temperature of terminal β, $\tilde{\kappa}_{\alpha\beta}$ is the thermal conductance between electrodes α and β, κ_{p0} is the thermal coupling of the probe to the ambient environment at temperature T_0, and κ_{ph} is the thermal conductance between the probe and a phonon bath with temperature T_{ph}. The environment could be, for example, the black-body radiation or gaseous atmosphere surrounding the circuit, or the cantilever/driver on which the temperature probe is mounted[11].

Using Eq. (1), the condition $I_p^Q = 0$ can be solved for the temperature of a probe in thermal and electrical equilibrium with, and coupled locally to the system

$$T_p = \frac{\tilde{\kappa}_{p1}T_1 + \tilde{\kappa}_{p2}T_2 + \kappa_{p0}T_0 + \kappa_{ph}T_{ph}}{\tilde{\kappa}_{p1} + \tilde{\kappa}_{p2} + \kappa_{p0} + \kappa_{ph}}. \qquad (2)$$

Here the thermal conductance $\tilde{\kappa}_{\alpha\beta}$ between electrodes α and β within the three-terminal thermoelectric circuit formed by the probe and hot and cold electrodes is[11]

$$\tilde{\kappa}_{\alpha\beta} = \frac{1}{T}\left[\mathcal{L}^{(2)}_{\alpha\beta} - \frac{\left[\mathcal{L}^{(1)}_{\alpha\beta}\right]^2}{\tilde{\mathcal{L}}^{(0)}_{\alpha\beta}} - \mathcal{L}^{(0)}\left(\frac{\mathcal{L}^{(1)}_{\alpha\gamma}\mathcal{L}^{(1)}_{\alpha\beta}}{\mathcal{L}^{(0)}_{\alpha\gamma}\mathcal{L}^{(0)}_{\alpha\beta}} + \frac{\mathcal{L}^{(1)}_{\gamma\beta}\mathcal{L}^{(1)}_{\alpha\beta}}{\mathcal{L}^{(0)}_{\gamma\beta}\mathcal{L}^{(0)}_{\alpha\beta}} - \frac{\mathcal{L}^{(1)}_{\alpha\gamma}\mathcal{L}^{(1)}_{\gamma\beta}}{\mathcal{L}^{(0)}_{\alpha\gamma}\mathcal{L}^{(0)}_{\gamma\beta}}\right)\right], \qquad (3)$$

where $\mathcal{L}^{(\nu)}_{\alpha\beta}$ is an Onsager linear-response coefficient, $\tilde{\mathcal{L}}^{(0)}_{\alpha\beta} = \mathcal{L}^{(0)}_{\alpha\beta} + \mathcal{L}^{(0)}_{\alpha\gamma}\mathcal{L}^{(0)}_{\gamma\beta}/(\mathcal{L}^{(0)}_{\alpha\gamma} + \mathcal{L}^{(0)}_{\gamma\beta})$ and $1/\mathcal{L}^{(0)} = 1/\mathcal{L}^{(0)}_{12} + 1/\mathcal{L}^{(0)}_{1p} + 1/\mathcal{L}^{(0)}_{2p}$.

We envision experiments performed in ultrahigh vacuum (UHV) with the electronic temperature probe operating in the tunneling regime and scanned across the sample at fixed height. The temperature imaged by this probe is a linear combination of the electron and lattice (phonon) temperatures. We assume that these two temperatures coincide in each bulk electrode but not in the graphene nanostructure itself. Under linear-response conditions, electron-phonon interactions and inelastic scattering are weak in graphene, so the indirect phonon contributions to $\mathcal{L}^{(0)}_{\alpha\beta}$ and $\mathcal{L}^{(1)}_{\alpha\beta}$ can be neglected. Thermal transport from phonons is included via κ_{ph}. The linear response coefficients needed to evaluate Eq. (2) may thus be calculated using elastic electron transport theory[27,28] $\mathcal{L}^{(\nu)}_{\alpha\beta} = \frac{1}{h}\int dE\ (E-\mu_0)^\nu\, T_{\alpha\beta}(E)\left(-\frac{\partial f_0}{\partial E}\right)$, where f_0 is the equilibrium Fermi-Dirac distribution with chemical potential μ_0 and temperature T_0. The transmission function[29,30] $T_{\alpha\beta}(E) = {\rm Tr}\left\{\Gamma^\alpha(E)G(E)\Gamma^\beta(E)G^\dagger(E)\right\}$ is expressed in terms of the tunneling-width matrices Γ^α and the retarded Green's function of the junction $G(E) = [\mathbf{S}E - H_{\rm mol} - \Sigma_{\rm T}(E)]^{-1}$, where the overlap matrix $\mathbf{S}$ reduces to the identity matrix in an orthonormal

basis and $\Sigma_{\rm T}(E) = -i\sum_\alpha \Gamma^\alpha(E)/2$. Throughout this work we consider transport in the wide-band limit where $\Gamma^\alpha(E) \approx \Gamma^\alpha$.

In the vicinity of the Dirac point, a simple tight-binding Hamiltonian has been shown to accurately describe the π-band dispersion of graphene[31]. The molecular Hamiltonian is $H_{\rm mol} = \sum_{\langle ij\rangle} t_{ij} d_i^\dagger d_j$ + H.c, where $t = -2.7$eV is the nearest-neighbor hopping matrix element between $2p_z$ carbon orbitals of the graphene lattice, and $d_i^\dagger$ creates an electron on the i^{th} $2p_z$ orbital. To be specific, we consider here a scanning thermal microscope (SThM) with an atomically-sharp Pt tip operating in the tunneling regime but near contact. The tunneling-width matrix may be described in general as[32] $\Gamma^p_{nm} = 2\pi V_n V_m^* \rho_p$, where n and m label π-orbitals of the graphene, $\rho_p(E)$ is the local density of states on the apex atom of the probe electrode, and V_m is the tunneling matrix element between the quasi-atomic apex wavefunction and orbital m of the graphene. We consider all s, p, d orbitals of the Pt SThM's apex atom and the π-system of the carbon sheet, meaning that the transport into the probe is multi-channel[32].

Results – The calculated local temperature distribution of a zig-zag GNR bonded to hot and cold electrodes held at T_1=325K and T_2=275K, respectively, is shown for several gate potentials and environmental coupling strengths in Fig. 2. In these calculations, the SThM is scanned 2.5Å above the plane of the carbon nuclei and the Γ matrices describing the lead-system coupling are diagonal. Non-zero elements of Γ, drawn as small red or blue circles in the figure, indicate contact between the electrode and the carbon atoms of the nanoribbon and are equal to 2.5eV. The probe is operating in the tunneling regime since the sum of Pt and C covalent radii is ∼2.03Å[33]. As indicated in the figure, the wavelength of the temperature variations changes as the quasiparticle energy is adjusted close to the Dirac point $\mu_{\rm Dirac}$.

In the simulations presented here, we consider both a weak environmental coupling κ_{p0}=$10^{-4}\kappa_0$, and a realistic environmental coupling κ_{p0}=$700\kappa_0$, where κ_0=$(\pi^2/3)(k_B^2 T/h)$ = 0.284nW/K is the thermal conductance quantum at 300K[34]. The weak coupling value κ_{p0}=$10^{-4}\kappa_0$ corresponds to the radiative coupling between a tip with effective radius ∼100nm and the blackbody environment, a fundamental limit on κ_{p0}[11]. At larger values of κ_{p0}, the amplitude of the quantum temperature oscillations is reduced due to the reduced sensitivity of the thermal measurement[11,20], but the qualitative features of the interference pattern are preserved. For comparison, the UHV SThM of Kim *et al.*[20] recently achieved κ_{p0}≈$700\kappa_0$. The phonon heat conductance κ_{ph} is small since the Debye frequency of Pt and the GNR's phonon distribution are incommensurate and, at 2.5Å above the GNR, the probe is not in contact with the GNR meaning that the thermal conduction across the vacuum tunneling gap into the probe is dominated by the electronic contribution. We consider a realistic value of κ_{ph}=$0.01\kappa_0$, and let T_{ph} vary linearly between the hot and cold electrodes. Although phonons carry considerable heat current in graphene[35], many different phonon wavelengths contribute to the heat transport at room temperature, washing out any coherent oscillations of the phonon temperature.

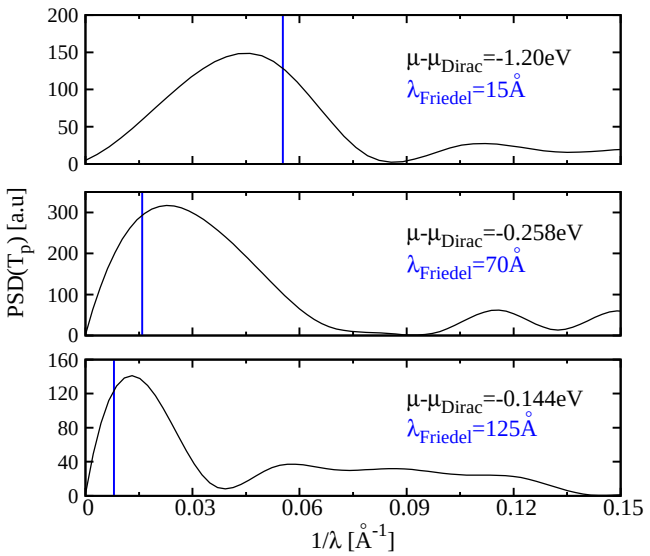

FIG. 3. The power spectral density (PSD) of a slice through the edge row of the GNR shown in Fig. 2 as a function of gate potential. The temperature oscillation wavelength increases as $\mu - \mu_{\rm Dirac}$ is decreased, in reasonable agreement with Eq. 4, whose values are indicated by vertical blue lines. The PSD spectra are complex because of the small size of the GNR, the multi-mode nature of the Pt SThM, and the phonon conductance. The temperature data within 10Å of each electrode have been neglected in the PSD spectra and $\kappa_{p0} = 10^{-4}\kappa_0$.

The spatial temperature variations are a consequence of quantum interference[10], where the flow of heat from the hot and cold electrodes into the probe is determined by position-dependent interferences and the molecular density of states[11]. According to Eq. (2), a maximally hot spot will be observed whenever $\kappa_{p1} \gg \kappa_{p2}$, and vice versa for a maximally cold spot. In general, the largest variations in temperature will be observed when the thermal conductance from one of the two electrodes into the probe is suppressed by destructive quantum interference[11], which occurs when the phase between thermal transport paths differs by π, so that $2k_F\Delta L = 2\pi$. Such $2k_F$ oscillations are ubiquitous in electron systems at low temperatures, the best known example being the Friedel oscillations in the density of states or charge density[22].

Due to its unique dispersion relation, the Friedel oscillation wavelength in graphene depends strongly on the energy of the quasiparticles, which may be controlled via the application of a gate voltage[22]

$$\lambda_{\rm Friedel}(E) = \frac{h v_{\rm F}}{2E}, \qquad (4)$$

where E is the energy away from the Dirac point. In our

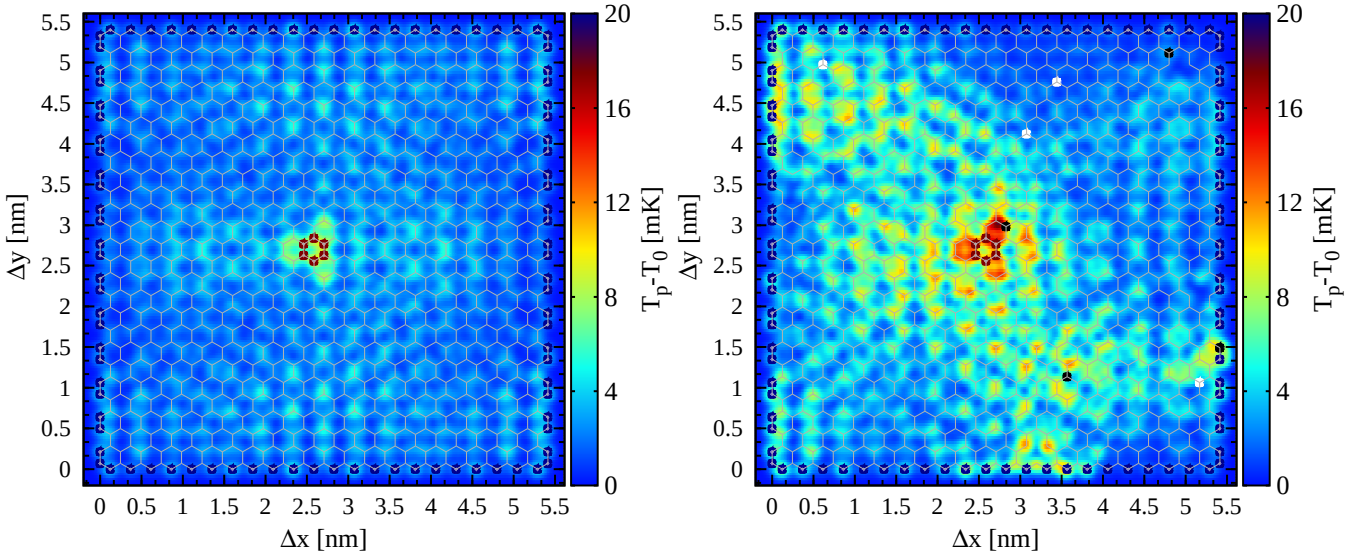

FIG. 4. The simulated temperature profile of a graphene fragment without (left panel) and with (right panel) impurities contacted by a hot (T_1=350K) needle electrode (the benzene-like contact pattern is indicated with red circles) and a 'cold' electrode (T_2=T_0=300K) bonded to the periphery of the sheet (blue circles) probed by a Pt SThM tip scanned 2.5Å above the plane of the carbon nuclei. In these simulations, we use κ_{p0}=700κ_0 (extracted from experiment) and κ_{ph}=0.01κ_0. The hot needle and periphery electrodes have per orbital coupling strengths of 1eV and 0.1eV, respectively. In the right panel, 0.33% boron (black circles), 0.33% nitrogen (white circles), and 0.33% vacancy impurities were included. Here $\mu - \mu_{\rm Dirac} = -1$eV.

tight-binding Hamiltonian $\hbar v_{\rm F} = 3ta/2$, where t=2.7eV is the tight-binding matrix element and a=1.42Å is the C-C distance[36]. The power spectral density (PSD) of a slice through the edge row of the GNR shown in the left panels of Fig. 2 is shown for $\mu-\mu_{\rm Dirac}$=-1.20eV, -0.258eV, -0.144eV (corresponding $\lambda_{\rm Friedel} \sim$ 15Å, 70Å, and 125Å, respectively) in Fig. 3. As shown in the figure, a spectral peak shifts as $\mu-\mu_{\rm Dirac}$ changes, in reasonable agreement with Eq. 4 (shown as vertical blue lines in the figure). Closer to the Dirac point, where the Friedel oscillation wavelength becomes comparable to the linear dimensions of the system simulated, it is not straightforward to resolve this peak above the background of peaks at small wavevectors arising from finite-size effects. Nonetheless, it is clear from Fig. 2 (lower panels) that the dominant wavelength of the temperature oscillations grows dramatically as $\mu \rightarrow \mu_{\rm Dirac}$. It should be emphasized that although the Friedel oscillations and the quantum temperature oscillations both have components at wavevector $2k_F$, there is no direct relationship between the equilibrium Friedel oscillations (local density of states oscillations) and the oscillations of the nonequilibrium temperature distribution (see Supporting Information).

The wide tunability of the temperature oscillations over orders of magnitude in wavelength in graphene indicates that they are within the spatial resolution of current SThM technology, which has achieved spatial and thermal resolution of 10nm and 15mK, respectively[20], provided the phase coherence length of the carriers is sufficiently long. In pure graphene the dominant dephasing mechanism is deformation potential scattering by acoustic phonons[37]. Using the scattering rate derived in Ref. 37 and assuming that the momentum relaxation time is equivalent to the phase-relaxation time, the phase-coherence length is given by

$$L_\phi(E) = \frac{4\hbar^3 \rho_m v_f^3 v_s^2}{D_{\rm A}^2 k_{\rm B} T E} \qquad (5)$$

where D_A is the deformation potential, v_{ph}=2×10^{6}cm/s is the acoustic phonon velocity, ρ_m ~7.6×10^{-8}g/cm^2 is the graphene ion mass density, and v_f ~1.53×10^{5}m/s is the Fermi velocity. The experimentally observed deformation potential ranges from 10-30eV. As an example, with D_A=30eV and T=300K, L_ϕ(1.0eV)=68.4nm and L_ϕ(0.05eV)=1.36μm. These estimates, which are in good agreement with recent experimental phase-coherence length measurements of graphene nanoribbons[38], clearly indicate that quantum thermal oscillations in graphene can occur on length scales well within the resolution of existing SThM techniques. Moreover, the electron-lattice cooling length is directly related to the inelastic mean-free path of the electrons given by Eq. 5, supporting the argument that electronic temperature oscillations can be observed in SThM measurements even with substantial phonon heat currents. Indeed, the more formidable experimental challenge is likely to be reducing the environmental coupling κ_{p0} of the probe to increase the amplitude of the thermal oscillations above the threshold for observation (cf. Fig. 2).

As a final example of an experimentally realistic system which may be used to investigate quantum temperature oscillations, we consider a graphene flake with a

hot needle-like terminal in the center, and the edge of the flake held at ambient temperature. The temperature profile for this junction is shown with and without impurities in the left and right-hand panels of Fig. 4, respectively, for $\kappa_{p0} = 700\kappa_0$–corresponding to the current experimental sensitivity[20]. In Fig. 4, we have taken $\mu - \mu_{\rm Dirac} = -1$eV; the predicted temperature profile exhibits a strong dependence on gate voltage and exhibits quantum oscillations within the resolution of current state-of-the-art SThM techniques. The temperature distribution in the right-hand panel includes a large total impurity concentration of 1%, split evenly between vacancies, boron adatoms (black circles), and nitrogen adatoms (white circles). The temperature oscillations are not destroyed by the addition of impurities, although the specific temperature wave pattern depends on the microscopic realization of disorder–serving as a fingerprint of the sample's impurity distribution. Adatom impurities are treated as onsite potential variations as discussed in Ref. 39. We stress that although computational resources have limited our discussion to small graphene structures, longer wavelength oscillations should be observable in larger systems provided the transport is phase coherent and coupling to the environment is minimized.

Conclusion – Using a realistic model of a scanning thermal microscope operating in the tunneling regime, we investigate the local electron temperature in graphene nanostructures subject to an applied thermal bias. We find that the wavelength of the temperature oscillations in these systems can be readily tuned via an applied gate voltage or doping, bringing quantum temperature oscillations within reach of the spatial resolution of existing measurement techniques for the first time. Graphene nanostructures are thus ideal systems for both fundamental and device related studies into the nature of temperature and heat transport at the nanoscale.

ACKNOWLEDGMENTS

Work by J.P.B. and M.A.R. was supported as part of the Non-Equilibrium Energy Research Center (NERC), an Energy Frontier Research Center funded by the U.S. Department of Energy, Office of Science, Basic Energy Sciences under Award DE-SC0000989. C.A.S. acknowledges support from the U.S. Department of Energy (DOE), Basic Energy Sciences under Award No. DE-SC0006699. M.D. acknowledges support from the DOE under Grant No. DE-FG02-05ER46204.

* justin.bergfield@northwestern.edu

[1] J. Altet, W. Claeys, S. Dilhaire, and A. Rubio, Proc. IEEE **94** (2006).
[2] J. Bischof, Heat Mass Transf. **42**, 955 (2006).
[3] Y. Chen, M. Zwolak, and M. Di Ventra, Nano Lett. **3**, 1691 (2003).
[4] Y. Ming, Z. X. Wang, Z. J. Ding, and H. M. Li, New J. Phys. **12**, 103041 (2010).
[5] M. Galperin, A. Nitzan, and M. A. Ratner, Phys. Rev. B **75**, 155312 (2007).
[6] Y. de Wilde, F. Formanek, R. Carminati, B. Gralak, P.-A. Lemoine, K. Joulain, J.-P. Mulet, Y. Chen, and J.-J. Greffet, Nature **444**, 740 (2006).
[7] Y. Yue, J. Zhang, and X. Wang, Small **7**, 3324 (2011).
[8] J.-J. Greffet and C. Henkel, Contemp. Phys. **48**, 183 (2007).
[9] H.-L. Engquist and P. W. Anderson, Phys. Rev. B **24**, 1151 (1981).
[10] Y. Dubi and M. Di Ventra, Nano Lett. **9**, 97 (2009).
[11] J. P. Bergfield, S. M. Story, R. C. Stafford, and C. A. Stafford, ACS Nano **7**, 4429 (2013).
[12] J. Meair, J. P. Bergfield, C. A. Stafford, and P. Jacquod, Phys. Rev. B **90**, 035407 (2014).
[13] M. Büttiker, Phys. Rev. B **40**, 3409 (1989).
[14] D. G. Cahill, W. K. Ford, K. E. Goodson, G. D. Mahan, A. Majumdar, H. J. Maris, R. Merlin, and S. R. Phillpot, J. Appl. Phys. **93**, 793 (2003).
[15] D. G. Cahill, K. Goodson, and A. Majumdar, J. Heat Transfer **124**, 223 (2002).
[16] Y. Dubi and M. Di Ventra, Phys. Rev. B **79**, 115415 (2009).
[17] Y. Dubi and M. Di Ventra, Phys. Rev. E **79**, 042101 (2009).
[18] K. Kim, J. Chung, G. Hwang, O. Kwon, and J. S. Lee, ACS Nano **5**, 8700 (2011).
[19] Y.-J. Yu, M. Y. Han, S. Berciaud, A. B. Georgescu, T. F. Heinz, L. E. Brus, K. S. Kim, and P. Kim, Appl. Phys. Lett. **99**, 183105 (2011).
[20] K. Kim, W. Jeong, W. Lee, and P. Reddy, ACS Nano **6**, 4248 (2012).
[21] F. Menges, H. Riel, A. Stemmer, and B. Gotsmann, Nano Lett. **12**, 596 (2012).
[22] J. Xue, J. Sanchez-Yamagishi, K. Watanabe, T. Taniguchi, P. Jarillo-Herrero, and B. J. LeRoy, Phys. Rev. Lett. **108**, 016801 (2012).
[23] Y. Dubi and M. Di Ventra, Rev. Mod. Phys. **83**, 131 (2011).
[24] D. Sánchez and L. Serra, Phys. Rev. B **84**, 201307 (2011).
[25] P. A. Jacquet and C.-A. Pillet, Phys. Rev. B **85**, 125120 (2012).
[26] A. Caso, L. Arrachea, and G. S. Lozano, Phys. Rev. B **83**, 165419 (2011).
[27] U. Sivan and Y. Imry, Phys. Rev. B **33**, 551 (1986).
[28] J. P. Bergfield and C. A. Stafford, Nano Lett. **9**, 3072 (2009).
[29] M. Di Ventra, *Electrical transport in nanoscale systems* (Cambridge University Press, 2008).
[30] J. P. Bergfield and C. A. Stafford, Phys. Rev. B **79**, 245125 (2009).
[31] S. Reich, J. Maultzsch, C. Thomsen, and P. Ordejón, Phys. Rev. B **66**, 035412 (2002).
[32] J. P. Bergfield, J. D. Barr, and C. A. Stafford, Beilstein J. Nanotechnol. **3**, 40 (2012).
[33] D. R. Lide *et al.*, ed., *CRC Handbook of Chemistry and Physics* (CRC Press, Boca Raton, Fla., 2005).
[34] L. G. C. Rego and G. Kirczenow, Phys. Rev. Lett. **81**, 232

(1998).
[35] A. A. Balandin, Nature materials **10**, 569 (2011).
[36] A. H. Castro Neto, F. Guinea, N. M. R. Peres, K. S. Novoselov, and A. K. Geim, Rev. Mod. Phys. **81**, 109 (2009).
[37] E. H. Hwang and S. Das Sarma, Phys. Rev. B **77**, 115449 (2008).
[38] S. Minke, J. Bundesmann, D. Weiss, and J. Eroms, Phys. Rev. B **86**, 155403 (2012).
[39] T. G. Pedersen and J. G. Pedersen, Phys. Rev. B **87**, 155433 (2013).